Engineering Structures 179 (2019) 225–245

Contents lists available at ScienceDirect

Engineering Structures

journal homepage: www.elsevier.com/locate/engstruct

Numerical investigation on the seismic dissipation of glazed curtain wall equipped on high-rise buildings

Lorenzo Casagrande[a,b,*], Antonio Bonati[b], Antonio Occhiuzzi[b,c], Nicola Caterino[b,c], Ferdinando Auricchio[a]

[a] University of Pavia, Civil Engineering and Architecture Department, Via Ferrata 3, 27100 Pavia, Italy
[b] National Research Council (CNR), Institute for Construction Technologies (ITC), Viale Lombardia 49, 20098 San Giuliano Milanese, Italy
[c] University Parthenope, Department of Engineering, Centro Direzionale Isola C4, 80143 Naples, Italy

ARTICLE INFO

Keywords:
High-rise buildings
Nonlinear dynamic analyses
Non-structural elements
Façades
Experimental tests
Hybrid systems
Glazed curtain walls
Steel Frame
Seismic performance

2010 MSC:
00-01
99-00

ABSTRACT

The dynamic interaction between glazed curtain wall stick systems and modern high-rise mega-frame buildings is investigated. In the present paper, four moment resisting frames (MRFs), consisting of thirty- and sixty-storey steel-based prototypes, are designed according to European standards: internal concentrically braced frame (CBF) core, outriggers and belt trusses are adopted to limit inter-storey drift and second order effects. Force-displacement relationships are derived from available full-scale test data performed on non-structural aluminium façade units. Therefore, 3D finite element (FE) models are developed to interpret the physical phenomena involved in façade dynamics: as a result, equivalent 1D nonlinear links are calibrated to simulate these phenomena independently. Nonlinear time history analyses (NLTHAs) are executed to investigate the potential combination of stiffness and strength of such hybrid systems, i.e. achieved through the integration of glazed curtain walls on the MRF lateral force resisting system (LFRs). Local and global performance will be shown in terms of inter-storey drifts and displacement peak profiles, forces and percentage peak variations, highlighting static-to-seismic load ratios in critical members and the sensitivity to the structural height. Conclusions point out that, even if accurately designed according to current standards, the façade omission from the seismic analyses of high-rise structures may lead to a crucial underestimation in the dissipation capacity of the building.

1. Introduction

Tall buildings have become the symbol of national economic welfare, restyling skylines and facing the scarcity of land, emphasized by the growing need for business and residential areas. A deeper insight on high-rise systems, innovative computational techniques, as well as high-strength and smart materials have led to exploration beyond traditional structural designs, posing novel challenges for civil engineers [1–3]. For instance, as the building height increases, longer periods and higher mode effects become dominant factors, demanding stiffness and stability design criteria instead of strength requisites [4,5]. Moreover, passive and active dissipation properties represent a supplementary principle in controlling the structural behaviour toward human comfort, safety and cost-effectiveness under lateral actions [6]. However, due to the broad nature of Codes, these necessarily reveal shortages in practical tools for structure-specific design [7–9]. Hence, ad hoc tools are required to predict and ensure the achievement of target performance levels. In fact, traditional approaches do not normally conduct toward an optimum in high-rise design: since uncertainties are commonly treated introducing simplifications in numerical modeling and analysis techniques, balancing the lack of confidence with weight coefficients that usually satisfy project requirements against economical needs [7,9].

Therefore, the use of scaled shaking table and wind tunnel testing, together with more conventional research tools such as finite element (FE) simulations, have been extensively adopted in dynamic response assessment [10,11]. Recently, the curiosity on non-structural elements has increased significantly, stimulated by the related reparation cost that commonly represents the highest investment, as highlighted in Fig. 1 and [12–15].

Accordingly, the novelty of this paper is in: (i) examining non-structural elements as a source of stiffness and energy dissipation, focusing on how they modify the dynamic structural response when coupled to the structural system; (ii) individually interpret the physical

* Corresponding author at: University of Pavia, Civil Engineering and Architecture Department, Via Ferrata 3, 27100 Pavia, Italy.
E-mail address: lorenzo.casagrande01@universitadipavia.it (L. Casagrande).
URLs: http://dicar.unipv.eu, http://www.itc.cnr.it (L. Casagrande).

https://doi.org/10.1016/j.engstruct.2018.10.086
Received 24 April 2018; Received in revised form 20 September 2018; Accepted 30 October 2018

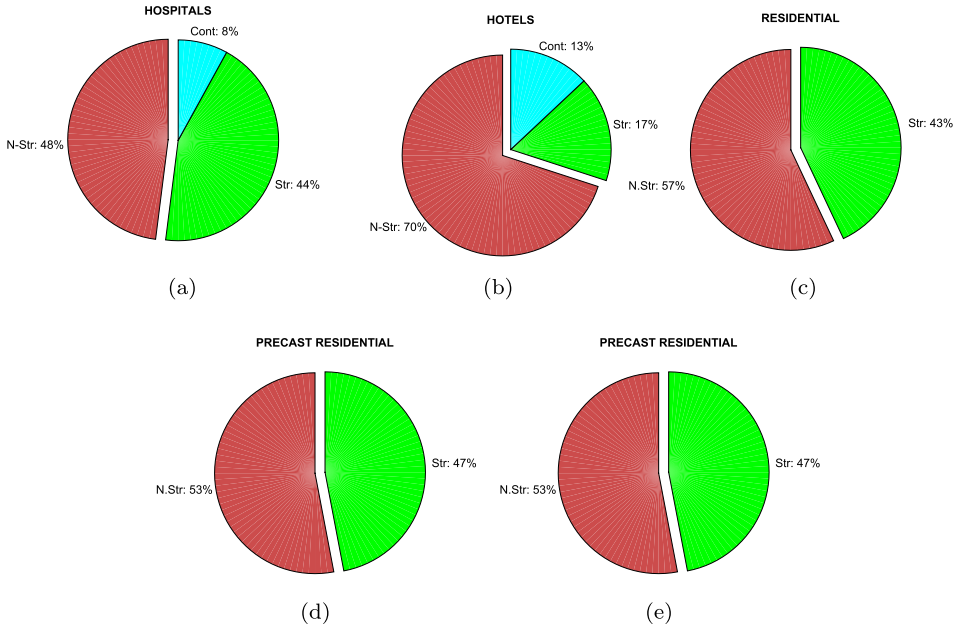

Fig. 1. Cost allocation in structural, non-structural and contents reparation.

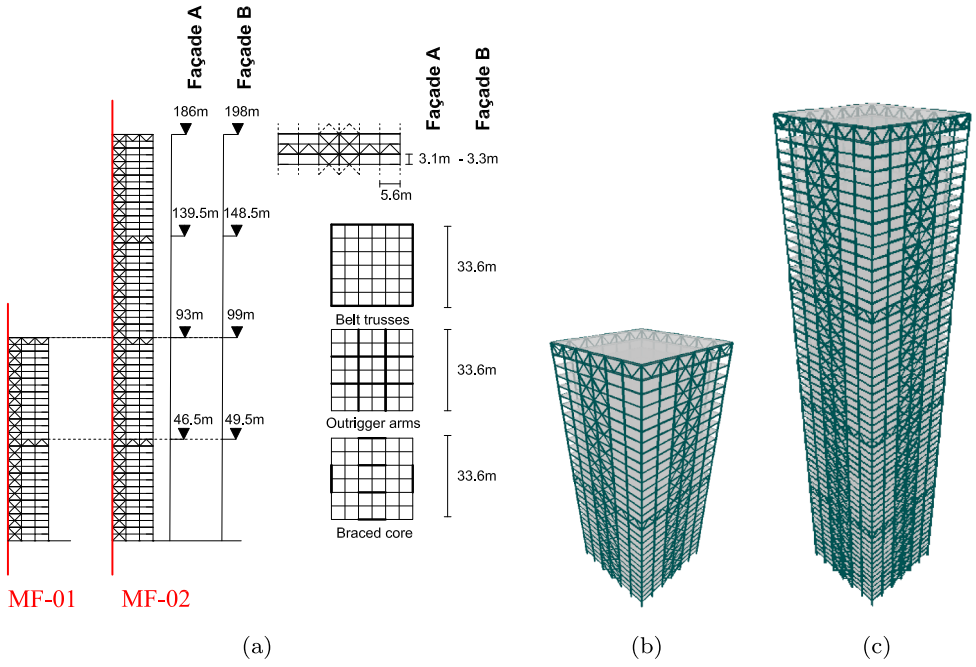

Fig. 2. Case-study buildings: plan and section geometries (a), MF-01, thirty-storey frame b), MF-02, sixty-storey frame (c).

mechanisms involved in façade response.

In particular, the widespread use of façades persuades researchers to focus on their seismic response, demonstrating the need in developing reliable methods to characterize the in-plane performance [16,17], and in presenting a complete FE modelling protocol [18]. Consequently, in the present paper a novel FE approach is developed to reproduce façade experimental results. Furthermore, the enhanced strength capacity obtained integrating the cladding in lateral force resisting systems (LFRS) of high-rise moment resisting frame (MRF) is explored.

The work is organized as follows. Section 2 describes the design of the reference high-rise MRFs and the tested façades. Section 3 explains the modelling stages for the selected structures (in Section 3.1) and curtain wall components (in Section 3.2), as well as the façade 1D model reduction (in Section 3.3). Section 4 discusses the observed

Table 1
Designed member details and grades of key structural components.

	MF-01			MF-02		
Façade A & B	Floor	Profile	Grade	Floor	Profile	Grade
Columns	1–5	HD 400X509	S450	1–20	HD 400X900	S450
	6–10	HD 400X421	S450	21–30	HD 400X634	S450
	11–15	HD 400X237	S450	31–40	HD 400X509	S450
	15–20	HD 400X237	S450	41–50	HD 400X314	S450
	21–30	HD 400X237	S450	51–60	HD 400X237	S450
Beams	1–30	IPE 400	S275	1–60	IPE 400	S275
Outriggers	15/30	HD 400X314	S700	15/30/45/60	HD 400X314	S700
Braces	1–5	HSS 300X16	S700	1–10	HSS 400X16	S700
	6–15	HSS 250X16	S700	11–20	HSS 350X16	S700
	16–30	HSS 200X16	S700	21–60	HSS 250X16	S700

modification of structural response due to façade interaction with the structural frame. Finally, Section 5 concludes the work presented.

2. Material and methods

Performance based design represents a prominent tool in plastic mechanism identification, seismic design and assessment of structures [7,8]. The crucial aspect lies in accurate hazard estimation, expressed as ground motion excitation, and consequently in defining the seismic demand and the MRF structural capacity [15]. This purpose is achieved through nonlinear static procedures (NSPs) or performing nonlinear dynamic time history analysis (NLTHAs). However, NSPs exhibit peculiar limitations in high-rise design [20,21], principally due to non-conservative inaccuracies in estimation of deformations for structures with significant higher-mode effects [22,23]. Therefore, since NSPs may not detect vulnerabilities during the change of dynamic properties after the first local mechanism [1,2], NLTHAs symbolizes the most attractive and rigorous approach in tall building design and assessment [3,24]. Nonetheless, NLTHAs require the definition of ground acceleration sets, increasing in complexity and computational cost with respect to NSPs. As a consequence, since 3D simulations would be excessively onerous to explore the full-scale MRF dynamic response, we model a planar frame FE structure with fiber-based members, capable of simulating structural components starting from their geometrical and mechanical attributes, as in [25,26] for welded and [27,28] for bolted joints.

From the non-structural perspective, to comprehend the complex mechanical phenomena underpinning the lateral response of façades, we reproduce the tested behaviour of the curtain walls through elaborated brick-based FE models. Subsequently, the goal is to couple a set of nonlinear zero-length fiber-based link elements [29], capable of rapidly predicting the experimental response of a façade system and potentially reduce the need for testing. Finally, in order to quantify the influence of cladding elements in structural dynamics, i.e. when these elements are considered acting on the lateral resisting frame system (LRFS), we obtain hybrid prototypes assembling non-structural links into structural MRF fiber-based models.

2.1. Description of the structure case studies

We choose four 6 × 6-bay planar prototypes (Fig. 2(a)), cut from reference 30- and 60-storey three-dimensional superstructures (Fig. 2(b)–(c), respectively MF-01 and MF-02), equipped with Façade A (height 3.1 m) and B (height 3.3 m). The LFRS is constituted by an internal 11.2 × 11.2 m concentrically braced frame core, coupled with orthogonal outriggers to reduce inter-storey drifts and second order effects. In both longitudinal and transversal directions, outriggers connect the internal to the perimetral braced core, redistributing inner loads; externally, one-storey high belt trusses ring the structure enhancing lateral stability. According to current European seismic provisions [30], we design the MRFs considering high seismicity (i.e. PGA = 0.40 g) on soil class C (i.e. 180 m/s < Vs < 360 m/s), choosing linear elastic structural models as the reference analysis technique, as recommended in 4.3.3.1(2) P of EC8 [30]. Dead and live loads are assumed to be 2 kN/m^2 and 4 kN/m^2, respectively, combined to permanent non-structural self-weights. The potential overcrowding load contribution is conservatively adopted as 60% quota of live loads. The horizontal wind pressure is calculated in accordance with ASCE-7 05 provision [31], considering the Basic Wind Speed equal to 37 m/s (84 mph). Using the SAP2000 software [32], we perform a series of response spectrum analyses (RSAs) to achieve the first-stage design, selecting q = 2 as behavior factor for V bracing systems in medium ductility class (DCM), and a complete quadratic combination (CQC) scheme according to [30].

We design HD tapered column profiles, welded gusset-plate and bolted beam-to-column connections according to [9,33], to comply with inter-story drift thresholds defining the serviceability limit state. The member sizes and grades are summarized in Table 1.

2.2. Description of the tested non-structural elements

This study focuses on the empirical data carried out at the Construction Technologies Institute (ITC) laboratories of the Italian National Research Council (CNR). The testing set-up is composed by a 5.720 × 7.370 mm steel frame, where three rigid trusses, adaptable to different curtain wall geometries, represent the main structure floors, Fig. 3. Horizontal displacements are applied to the beams, imposing equivalent seismic-induced lateral drifts as previously in [35,36], accordingly with the Crescendo Test of American Standards, AAMA 501-6 [37]. The dynamic assessment of two full-scale glazed curtain wall stick systems is investigated, comparing the crescendo test results with past researches [35,36] and worldwide code prescriptions [37–39].

2.2.1. Façade specimens: description, experimental activity and results

The two tested façade units, named Façade-A and Façade-B, refer to the experimental data outlined in [19], where exhaustive test details are provided. In Table 2, the mutual material classes and technical details are summarized. In particular, the aluminium EN-AW 6060-T6 with Young Modulus E = 69 GPa is used, while E = 70 GPa tempered glass characterizes insulated glazed units. Silicone gaskets support the glass panels along the edges, avoiding the direct contact between panels and aluminium frames, with a clearance of 5 mm. Continuous mullions support suspended transoms.

Quasi-static force control tests are performed, pushing the intermediate steel beam toward a specific inter-storey drift demand (as the relative displacement between outer rigid beams of the supporting structure). In Façade A, the threshold displacement imposed at 1.6% of the inter-storey height is achieved at the fourth cycle: reducing the lateral load (applied by the actuator and measured by a 50 kN LeBow load cell), a residual 32.2% of cycle peak drift is recorded.

Large shear deformations affect the aluminium frame, causing the

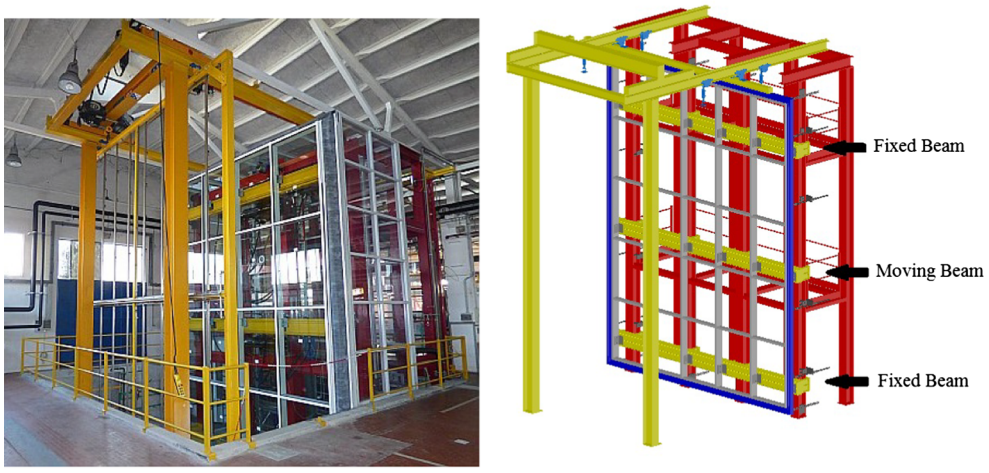

Fig. 3. Testing setup - global view (a) and detail of rigid beams (b).

Table 2
Details and geometrical data of Façade A and Façade B.

Attributes		Façade - A	Façade - B
Geometry	*Height*	7291 mm	7262 mm
	Width	5641 mm	5630 mm
	Inter-storey	3100 mm	3300 mm
Element number	*Mullions*	4	5
	Transoms	4	6
	Glazed Panels	12	23
Transom-to-Mullion joint	*Connection*	T-joint	C-joint
Tempered glass panels	*Thickness*	8 + 16 + 8 mm	8 + 8.2 + 16 + 6 mm
	Geometry	5720 × 7370 mm	5720 × 7370 mm
Supporting structure	*Connection with façade*	Rigid	Rigid
	Rigid beam spacing	3100 mm	3300 mm

expulsion of the largest glass panel from its frame location, Fig. 4(a). In Façade B, 1.08% inter-storey drift is recorded without glass fall. The elastic-to-plastic transition phase is reached in the first cycle, where the 70.9% of the peak residual displacement is recorded Fig. 4(b).

3. Calculation: Finite element modelling scheme

In this section, we propose a four-stage modelling approach toward the dynamics evaluation of the coupled system: these are obtained through the union of the structural frames and non-structural façades. In the first stage (Section 3.1) we develop nonlinear fibre-based numerical models of the two reference structures: the MRFs are exposed to NLTHAs, based on a set of ten natural records scaled by [40] and spectrum-compatible in displacement in accordance with EC8 prescriptions [30]. In the second stage (Section 3.2), we reproduce the tested response of curtain walls through 3D full-scale advanced models, with particular emphasis to the gasket role in influencing the cyclical reaction of façade A Fig. 4(a) and B 4(b). In the third stage (Section 3.3), we present equivalent 1D nonlinear links, able to predict the dynamic response of curtain walls, lightening computational effort and potentially reducing expensive experimental tests. In order to examine the effectiveness of non-structural elements when applied to mega-tall buildings, in the fourth-stage (Section 3.4) we integrate the 1D equivalent links to the first-stage structural models, i.e. generating hybrid systems. Finally, we perform a new series of NLTHAs to foretell the changed dynamics.

3.1. First Stage: fibre-based structural models

As aforementioned in Section 2.1, we develop the FE representation of the thirty- and sixty-stories structural prototypes into the open source platform OpenSees [41]. Moreover, by means of fibre-based idealizations we consider geometric and material nonlinearities through corotational transformation and distributed plasticity. The modeling technique is generated based on mechanical idealizations gathered from [9], accounting for Menegotto-Pinto [42] plasticity propagation in force-based structural members, possible buckling mechanisms in braces and gusset plates, tangent-stiffness proportional Rayleigh damping [43], and detailed simulation of bolted and welded connections derived from geometrical and mechanical attributes, according to [26–29]. Lastly, NLTHAs are performed selecting ten natural records, in Table 3 and Fig. 5, scaled by Maley et al. [40] to achieve spectrum compatibility in displacement to the reference EC8 Type 1 - Soil C spectrum (as in EC8 [30]).

3.2. Second Stage: brick-based non-structural models

The high-definition numerical models introduced herein are intended to reproduce the dissipative behavior of the two full-scale tested glazed curtain walls. In particular, we examine four parameters as accountable for the overall force-displacement response: (i) the transom-to-mullion constraint and its rotational stiffness; (ii) the gap among aluminum frame members and glass panels; (iii) the mechanical local interaction between glass and frame; (iv) the physical behavior of gaskets [19]. In a computational time-saving approach, we developed

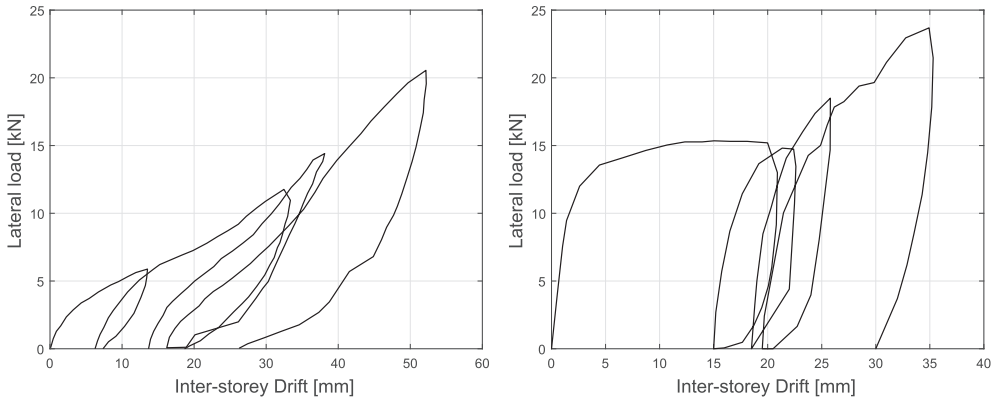

Fig. 4. Force-drift cyclic test results: Façade A (a) and B (b) (after Caterino et al. [19]).

Table 3
Natural ground motion records, after Maley et al. [40].

ID	PEER ID	Event	Component	Mw [−]	D [km]	t_{tot} [s]	V_s [m/s]	SF[−]
01	1233	Chi-Chi, Taiwan	E	7.62	36	90	194	2.1
02	1153	Kocaeli	090	7.51	127	102	275	7.9
03	851	Landers	000	7.28	157	70	272	4.0
04	1810	Hector	090	7.13	92	60	345	2.9
05	1629	St Elias, Alaska	279	7.54	80	83	275	1.5
06	777	Loma Prieta	090	6.93	28	39	199	1.8
07	1043	Northridge-01	090	6.69	52	48	309	5.8
08	728	Superstition Hills-02	180	6.54	13	40	194	2.3
09	172	Imperial Valley-06	140	6.53	22	39	237	5.1
10	2615	Chi-Chi, Taiwan-03	N	6.20	40	107	273	5.6

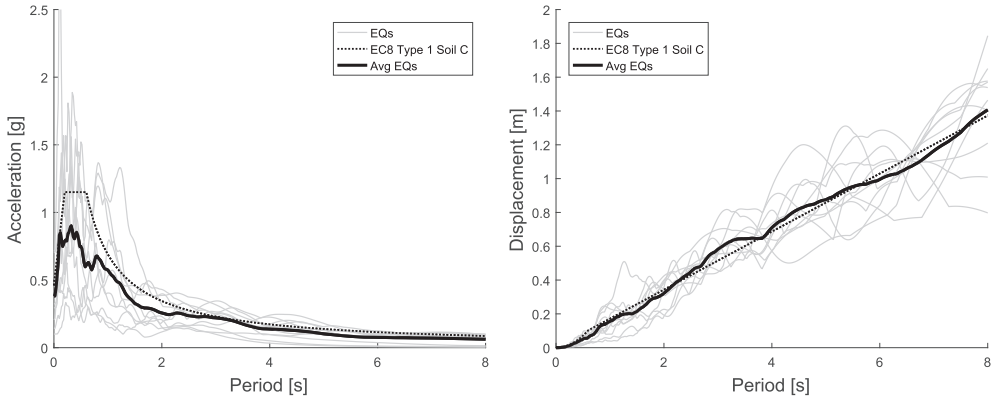

Fig. 5. Reference acceleration and displacement spectrum (after Maley et al. [40]).

three-dimensional local models of mullion-to-transom and glass-to-frame connections in order to extrapolate the cyclical elasto-plastic performance and gain knowledge on the stiffening nature of the joints. Subsequently, we assume equivalent nonlinear constraint elements assembled on a reference three-dimensional full-scale façade model, accurately reproducing the rotational stiffness and the plastic dissipation of transom-to-mullion and glass-to-gaskets knots. The ABAQUS 6.14 software [44] is adopted to play out the FE simulations, interpreting the influence of bounded mechanisms and their interactions in the overall response.

We adopt first-order 8-node linear elements (C3D8R) in a three-dimensional isoparametric framework, accounting for geometrical and material nonlinearities, finite strain and rotation in large-displacement analyses. Reduced integration Barlow points and Flanagan/Belytschko hourglass control methods [45] are contemplated likewise. General nonlinear contact conditions, including the coupled effect of friction, slip and impacts are considered. In order to accurately replicate the aluminium stress-strain behaviour and the permanent deformations

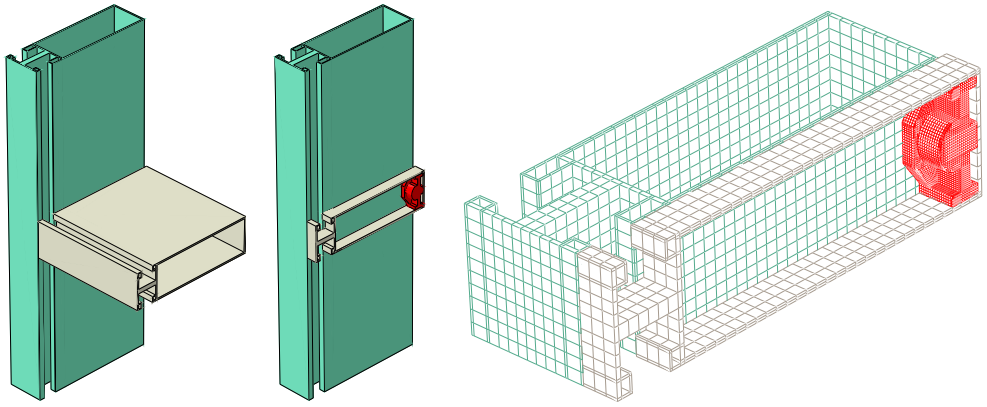

(a) (b) (c)

Fig. 6. Façade A - Transom-to-mullion connection (a-b) and T-joint mesh (c).

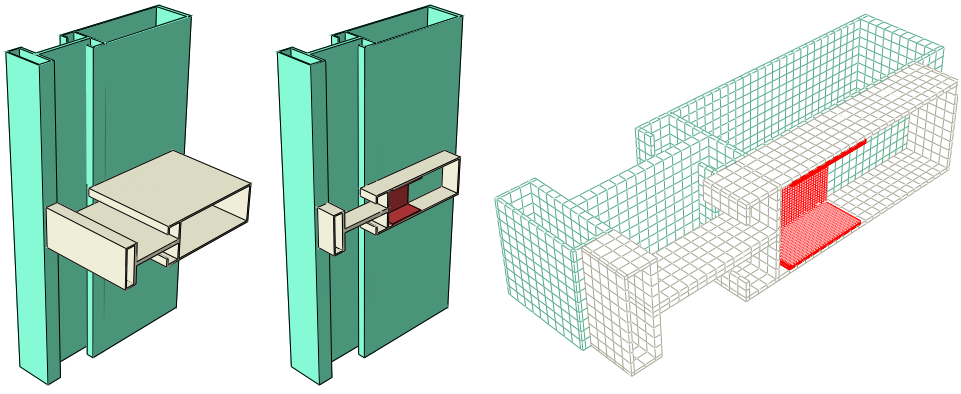

(a) (b) (c)

Fig. 7. Façade B - Transom-to-mullion connection (a-b) and U-joint mesh (c).

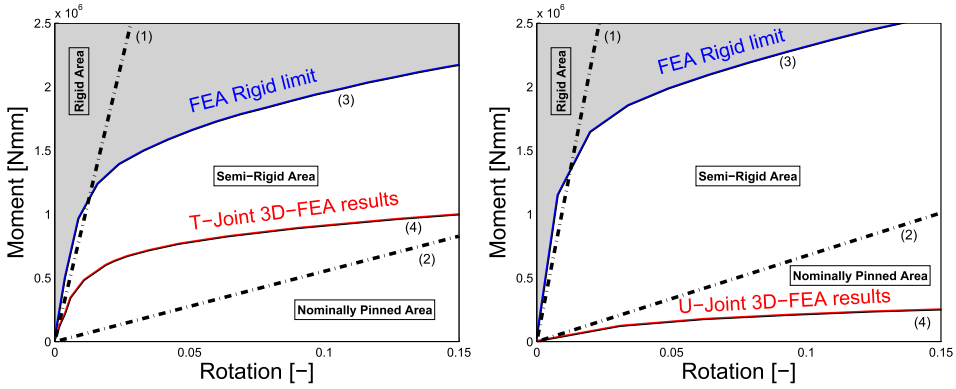

(a) (b)

Fig. 8. Transom-to-mullion moment-rotation curves: Façade A (a) and Façade B (b).

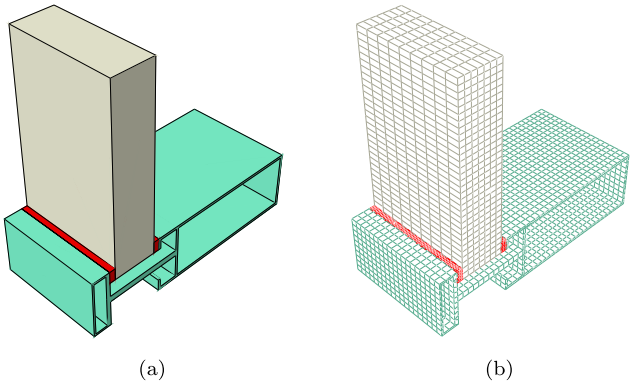

Fig. 9. Glass-to-frame connection (a) and gasket mesh (b).

achieved in the loading-unloading history, the rate-independent Von Mises yielding principle for metal plasticity is adopted, associated with isotropic strain hardening. Transom-to-mullion connections are composed by T- and U-joint steel systems (Figs. 6 and 7), respectively in Façade A and Façade B, as described in [19] and Table 2. Since geometric details differentiate the joint rotational stiffness, we run a meticulous parametric campaign to classify the connections according to EC3 [46] prescriptions, i.e. comparing the rotational stiffness $S_{j,ini}$ with:

- *Zone*1: *Rigid* $S_{j,ini} \geqslant k_b EI_b/L_b$
- *Zone*2: *Semi* − *Rigid* $k_b EI_b/L_b < S_{j,ini} < 0.5EI_b/L_b$
- *Zone*3: *Nominally* − *Pinned* $S_{j,ini} \leqslant 0.5EI_b/L_b$

In Fig. 8: (1)-(2) curves represent EC3 [46] limits classifying Rigid, Semi-Rigid and Nominally Pinned zones, (3) is the contextual rigid boundary obtained considering a fully-fixed joint in models and (4) is the specimen moment-rotation curve achieved by 3D FE analyses. While the T-joint connects mullions to transoms in a very stiff way regarding relative displacements (Fig. 8(a)), the U-joint results to be less stiff, allowing rotations through the bending of the thin aluminium walls (Fig. 8(b)). As aforementioned, since the behaviour of the two tested façade units is determined by the interaction of their sub-assemblies, the difference in transom-to-mullion rotational stiffness directly contributes to influence the dissimilarity in Façade A and B responses.

Fig. 9 shows the FE approach developed for the glass-to-gaskets interaction.

Additionally to the former modeling assumptions, constitutive laws for glass and gaskets are herein defined. According to Memari et al. [35], we consider the glass panel as an equivalent full-section member (data in Table 2), with three-dimensional isotropic elements (C3D8R), prone to evaluate the peak stress responses: elasto-plastic material relationships are therefore calibrated to reproduce the strain of the gasket and the glass-to-gasket nonlinear frictional effects. Moreover, the stiffening enhancement due to the glass-to-frame impact along the glass panel boundary, main cause of glass fracture as highlighted in [17,35], is implemented into gasket constitutive laws by a FE parametric campaign.

In detail, trough dedicated sensitivity analysis we find that the gasket elastic stiffness influences the slope of the initial branch in the overall response (Fig. 10(a)–(c)) and the gasket yielding provokes the shift to the non-linear plastic branch, causing the trigger of glazed panel sliding (Figs. 10(b)–(d)). Accordingly, we stress here the importance of the gasket performance into the backbone response of curtain wall tests. Differently form [19], the need to explicitly considers each façade contribute separately is fulfilled in Section 3.3 where we introduce a 1D shear link that rapidly replicate tested and FEA results (Fig. 11).

Typically, in order to properly identify the higher stress-strain distribution in connective elements, i.e. on the T/U-joints (Figs. 6 and 7) and on the gaskets (Fig. 9), 10 times finer mesh density is considered in these members. We reproduce the experimental loading protocol, adopted during the test, through an implicit solution strategy and imposing the energy-normalized convergence criterion limit to 10^{-3}, according to [47]. Additionally, the contact prerequisites between the mullion-to-transom connection elements are defined by means of master-to-slave interfaces, permitting the relative sliding interaction. Otherwise, gasket and glass panels are assumed to be clamped to each other, since gasket pre-compression prevented relative displacements. As aforementioned, equivalent 1D nonlinear links are adjusted to model the mechanical behaviour of the red-colored tie elements, displayed in Figs. 6–9, lightening the computational process and refining the time management.

3.3. Third Stage: 1D non-structural modelling reduction

Most of the FE beam approaches gain their benefit in decreasing the computational cost; however, the model accuracy tends to be highly sensitive to the nature of the numerical simplifications [47]. Otherwise, detailed three-dimensional brick-element simulations may extensively describe the investigated processes, but greatly increasing the computational time [22]. Besides, broad efforts in full-scale façade model reduction can be legitimize by the development of efficient and meticulous procedures in nonlinear dynamic response prediction, reducing the need of expensive laboratory tests and providing a practical support to professionals and researchers [7]. To this aim, founded on the exhaustive observations collected by ITC during its decennial collaboration with curtain wall producers, we develop an equivalent 1D link element applicable in the comprehensive dynamic façade response prediction.

Fig. 12 illustrates the conceptual schematic of the mono-dimensional shear spring model, obtained combining non-linear links that separately represent the four mechanisms that characterize the curtain wall lateral response, such as the aluminum frame deformation, the gasket distortion, the glass-to-frame gap and the energy loss due to the glass-to-frame impact. Due to the parallelism of the zero-length two-nodes links, the proposed model results to be adaptable to changes in stick system geometry and inter-storey height variability.

In this regard, input parameters are derived through iterative numerical calibration (in Section 3.2) and individually represented by zero-length two-nodes links. In detail, we assign to these elements the following constitutive models:

- *Viscous Gasket Links*: governed by stiffness (k), damping coefficient (C_d) and velocity exponent (α);
- *Elastoplastic Impact Links*: controlled by relative tangent stiffness (E), yield force (F_y) and hardening ratio (η);
- *Elastoplastic Frame Links*: Bouc-Wen regulated by initial elastic stiffness (k_0), yield force (F_y), ratio of post-yield stiffness (r), control shape of hysteresis loop (γ, β), control of tangent stiffness (A_0, δ_A) and control of material degradation (δ_ν, δ_η).

In particular, while the physical parameters of the gasket are derived (from Fig. 10), and rigid glass-to-frame interactions can be assumed after the gap closure (Table 4), the Bouc-Wen link parameters should be derived from mathematical models [48,49], from ad hoc numerical simulation, such as Fig. 8(a) and (b), or from experimental

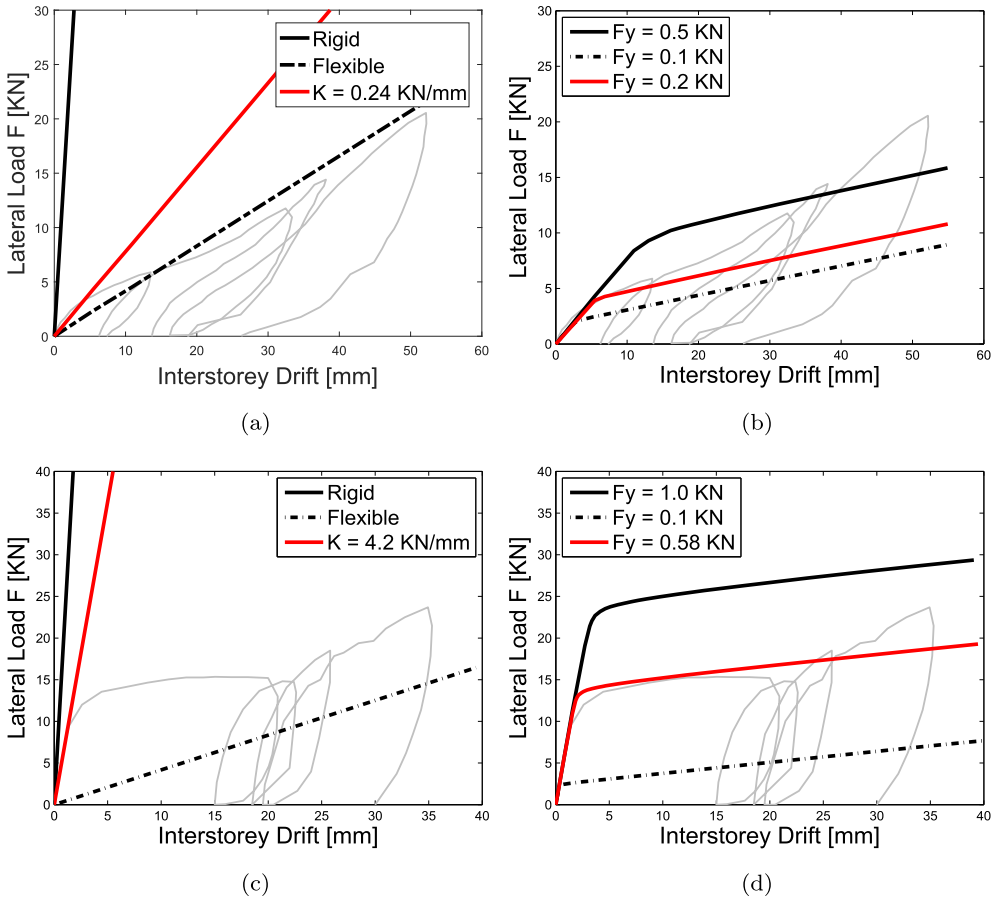

Fig. 10. Sensitivity analysis: FAÇADE A (a) gasket elastic stiffness, (b) gasket plastic regime; FAÇADE B (c) gasket elastic stiffness, (d) gasket plastic regime.

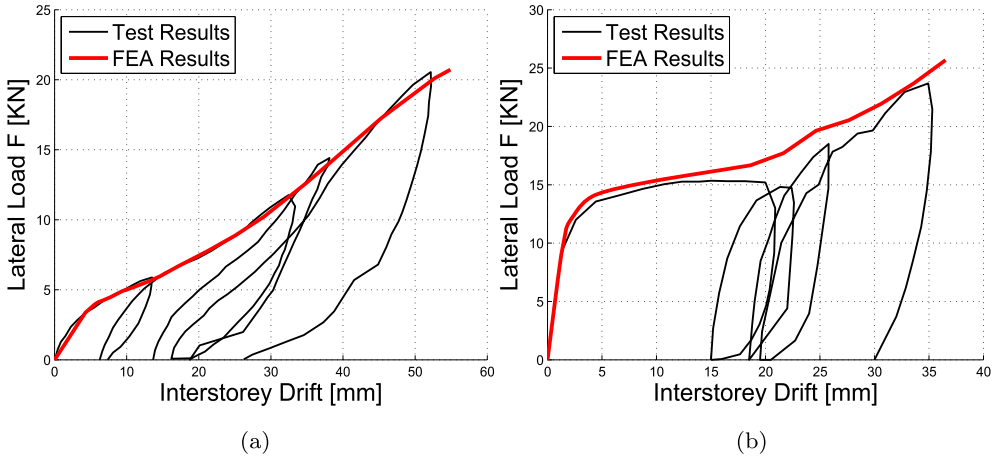

Fig. 11. Force-drift cyclic results from testing & modeling: Façade A (a) and Façade B (b).

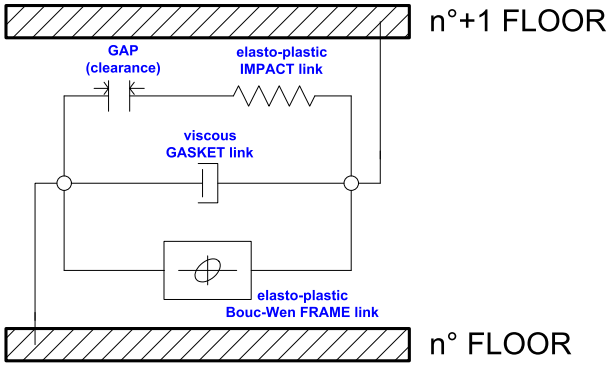

Fig. 12. Schematic of the 1D equivalent façade shear spring model.

Table 4
Calibrated parameters of Façade A and Façade B, from Fig. 10.

	FAÇADE A	FAÇADE B
Transom-to-mullion joint stiffness (Bouc-Wen from)	Fig. 8(a)	Fig. 8(b)
Transom-to-mullion connector number	30	54
Glass-to-frame yield force (Fy)	0.20 KN	0.58 KN
Local impact stiffness (E)	10 KN/mm	10 KN/mm
Glass-to-frame gap	3 mm	5 mm
Gasket elastic stiffness (k)	0.24 KN/mm	4.2 KN/mm
Gasket damping coefficient (Cd)	0.11 KNs/m	0.15 KNs/m

evidences. In Fig. 13, the 1D modeling outcomes performed in OpenSees, the testing data and the 3D FE results are overlapped. Numerical simulations exhibits a rigorous agreement regarding the initial stiffness, the inter-story peak drifts and the shear resistance, as well as the global ductility and the elastic-to-plastic transition.

3.4. Fourth Stage: hybrid modeling

Recent developments in performance-based earthquake engineering (PBEE) have highlighted that the compliance between structural and non-structural performance represents a crucial aim against vulnerability reduction and toward functionality level achievement [7,8]. However, no rigorous guidance in seismic codes has been provided regarding interactions between structural and non-structural systems [15]. Eurocode 8 [30], ASCE7-05 (2005) [31] and NZS1170.5 [50] supply formulae to estimate equivalent static design forces, corresponding to the inertial loads on the secondary components, commonly a function of the mass, the period of vibration, the peak ground acceleration and component location. Nonetheless, although the aspiration to develop a rational method, current approaches may not always be reasonable, ignoring the ground motion input nature, the effect of higher modes in supporting structures and the effect of non-linear response [15]. Contemporary practical design cases are mainly dealt through decoupled analyses, conducted by cascade approaches in which the dynamics of the structure and the floor accelerations are measured without considering the interaction between the primary structure and non-structural components [15]. In this regard, the Floor Response Spectrum (FRS) method represents a widely used approach. However, the vibration of any secondary element may alter the dynamics of its supporting structure, causing modifications in the secondary element response itself. Consequently, the dynamic characters of both the structural and non-structural components, should be assessed in advance [51]. Beyond the inaccuracy in omitting the transient dynamic interaction, i.e. assuming practical values of inherent elastic damping by consensus [3], the beneficial effect of non-structural component dissipation cannot be evaluated. In fact, structural damping represents only a portion of the dissipative properties of a building, since in serviceability limit state the main physical sources of energy dissipation are usually provided by the structure, by the foundation level and by drift-sensitive non-structural elements [7].

Moreover, even though in the last decade the ambition was to establish an analytic method for non-structural seismic design, according to [15] none of these seemed to be appropriate for seismic guidelines, mainly due to the:

- massive amount of degrees-of-freedom in dynamic analyses for structural and non-structural interaction; furthermore, to accurately consider this interplay, step-by-step NLTHAs should be performed;
- diffuse support excitation provided by multiple anchorages that connect secondary elements to the structure;
- asynchronous design of structural and non-structural elements;
- circumstance of tuned natural frequencies between the secondary components and the structure, inducing highly correlated modal responses.

Drift-sensitive non-structural elements can perturb the structural seismic response, increasing the stiffness and the energy dissipation: therefore, the proposed methodology aim to quantify the global seismic response implementing equivalent 1D links (Figs. 12 and 13) between each storey of the structure (for symmetry, the calibration is adapted to represent floor-by-floor response, Fig. 14). Differently from the traditional area-based approaches, such as the EVD method [7] in which the non-structural energy dissipation is approximated by an equivalent viscous damping source, the proposed methodology wants to add a more precise equivalent model to the structure, emulating the whole physical phenomena behind the non-structural response. Accordingly, the suggested technique tends to address the aforementioned shortcomings in traditional PBEE methods through an extremely flexible and simplified approach, tracking in a consistent way the evolution of local damage and the dissipation amount. In detail:

- no sensitive degrees-of-freedom increment in structural/non-structural element interaction; the good agreement in static-to-dynamic results makes time history, response spectrum and pushover analyses reliable;
- façades are drift-sensitive non-structural units: since multiple anchorages fasten continually the façades along the floor slabs, it is pertinent consider the non-structural link activation related to the inter-storey drifts;
- on one hand, façades represent the weak element of the hybrid model, directly undergoing the inter-storey drift of the structure; on the other hand, these can affect the global lateral sway: as a result, the compliance to drift limitations shall be considered, according to [30,31,34,37–39];
- developments in Building Information Modeling (BIM) exhibits its potential in construction management, mainly due to different protagonist interaction for time-varying structures. As a result, it is expected that asynchronous design processes would generally decrease;

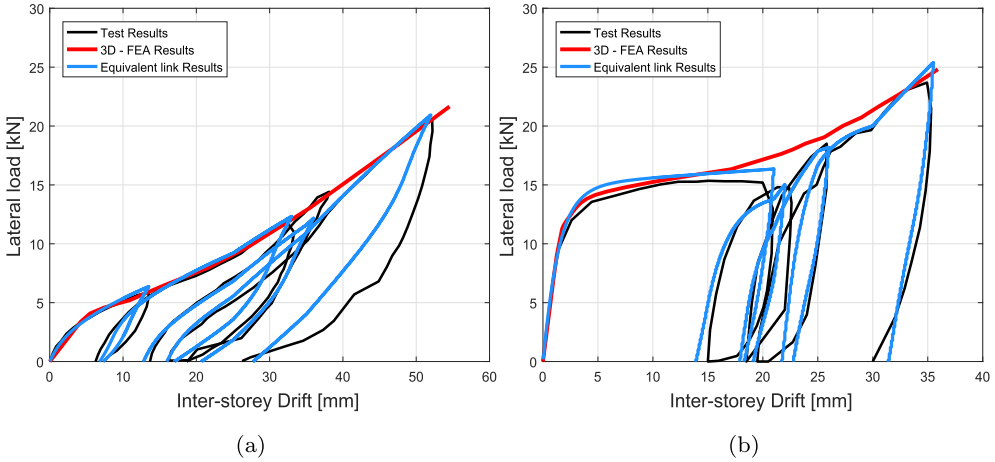

Fig. 13. Force-drift cyclic results from testing & modeling: Façade A (a) and Façade B (b).

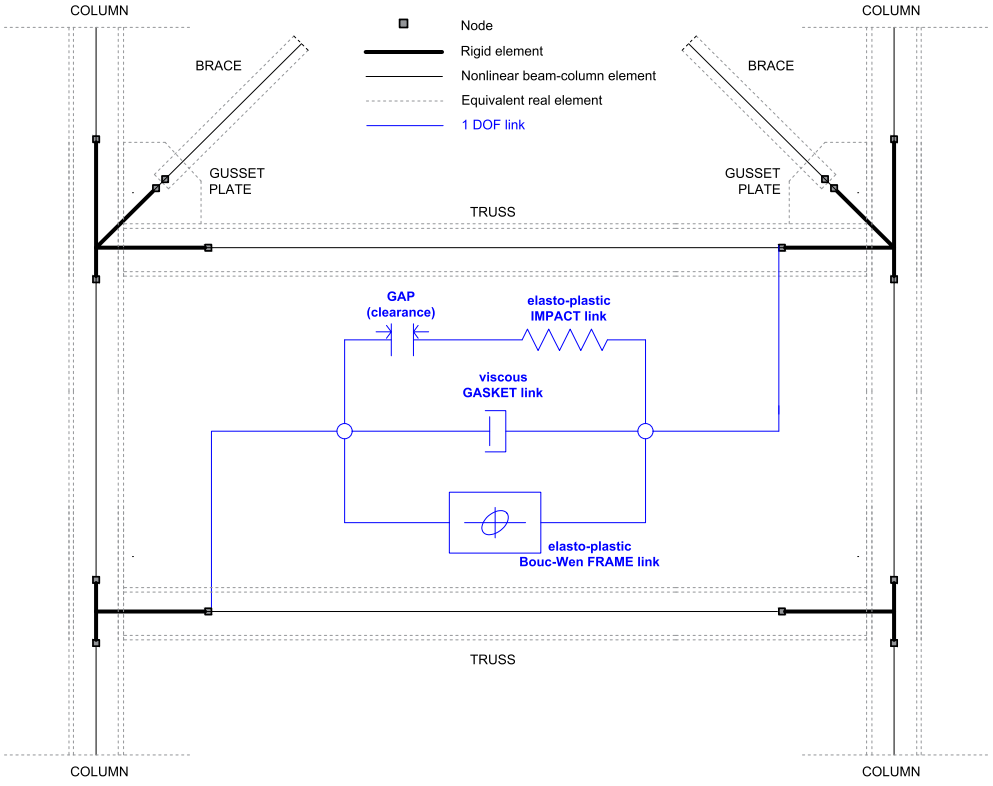

Fig. 14. Equivalent 1D link implemented on the structure.

- high frequency ranges characterize traditional façades (5–200 Hz, [52,53]), while lower frequencies distinguish primary civil structures. Therefore, frequencies tuning occurrence is not expected.

4. Results and discussion

We conduct NLTHAs undergoing the two reference high-rise structures to ten natural records, considering on one hand the bare MRF case, on the other hand the combined response between MRF and tested façade. Initially, individual earthquake response on the bare frame ("EQs", in diagrams), their average ("MRF", in diagrams) and NLTHAs average obtained considering the cladding ("NLTHa Avg", in diagrams) will be shown. Subsequently, the percentage variation between average values, MRF and NLTHa Avg, will be exhibited, highlighting the influence of glazed curtain wall stick systems in affecting both the local and the global structural performance. FAÇADE A and B, evoked in figure captions, specifies the curtain wall typology assumed.

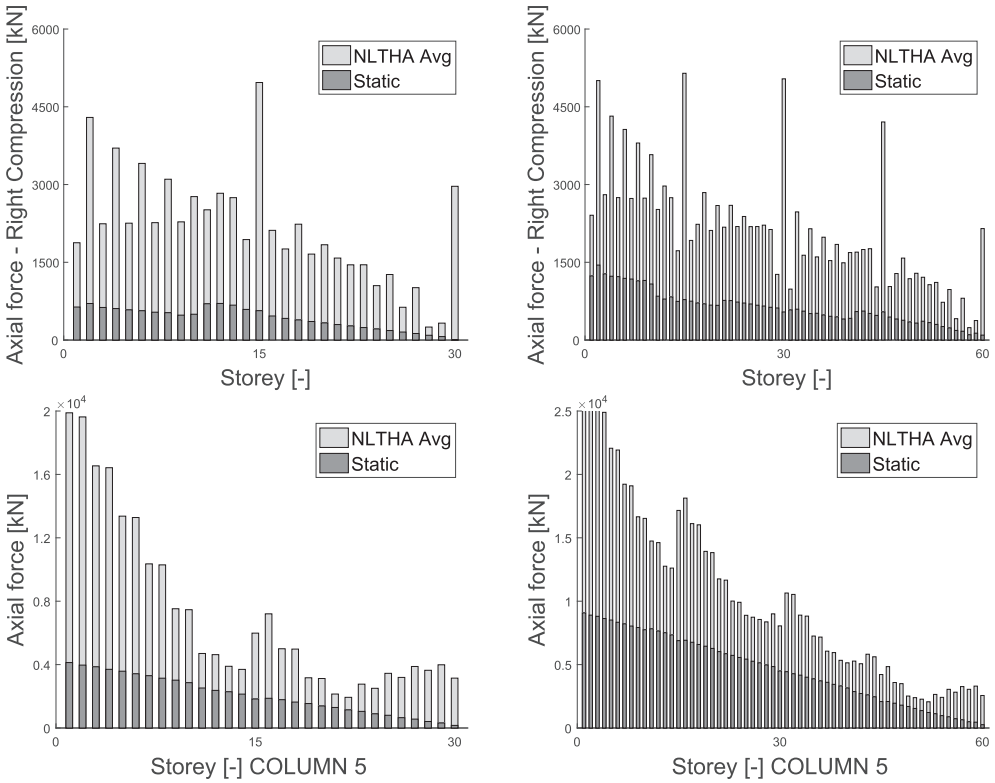

Fig. 15. Static-to-seismic axial load ratio in braces and rightmost core columns, MF-01 (left) and MF-02 (right).

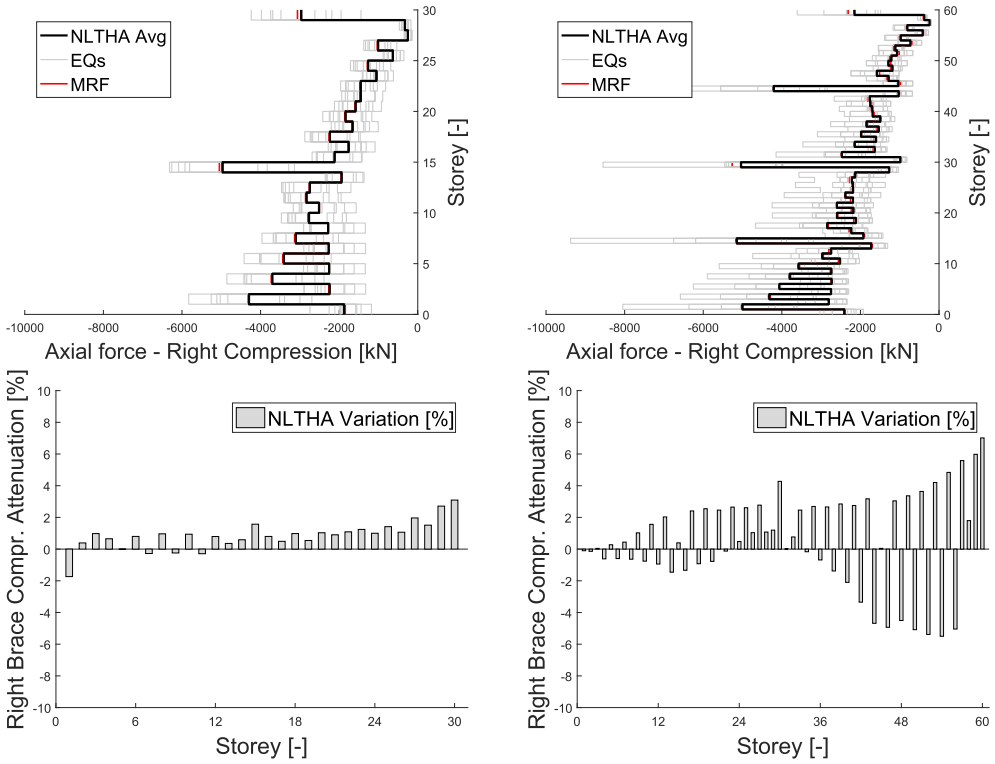

Fig. 16. FACADE A - Axial force profile in reference braces & compression variation, MF-01 (left) and MF-02 (right).

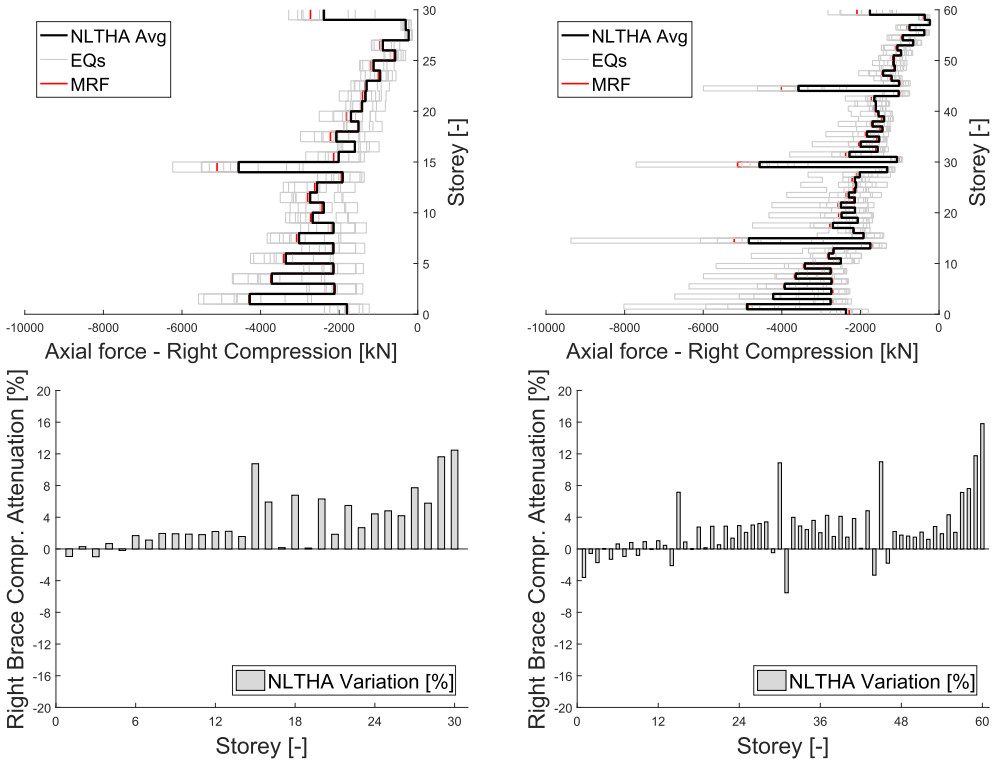

Fig. 17. FAÇADE B - Axial force profile in reference braces & compression variation, MF-01 (left) and MF-02 (right).

4.1. Local performance

Thereafter, force and displacement diagrams are specified for MF-01 and MF-02 prototypes, both for façade A and B; percentage variations, representing the attenuation achieved by fastening façades on the building, are consequently calculated from MRF and NLTHAs Avg diagrams. Fig. 15 displays the axial seismic overload in critical components, i.e. highlighting the extent of seismic actions absorbed by braces and columns, compared to permanent loads. In accordance with the findings of Brunesi et al.[9], the in-plane rotation of the structure lead to an earthquake-induced compressive overburden in the leftmost and rightmost core columns, in comparison with the central ones that remain approximately unaffected. Therefore, force concentrations occur in outrigger levels due to the synergism between stiffness and floor acceleration.

Hence, the outrigger contribution to the lateral resistance results in the transmission of seismic overloads, from floors to core columns. As a result, only values in core braces (Figs. 16 and 17), in the outrigger spans (Figs. 18 and 19) and in the rightmost core columns (due to structural symmetry, Figs. from 20–25) will be displayed hereafter, representing critical members.

Brace peak axial forces are located in correspondence to the 15^{th} storey (5039 kN for façade A and 4482 kN for façade B, as in Figs. 16 and 17 and Table 5); the same peak values are directly absorbed from the adjacent outrigger (15° Outrigger Axial Force, Table 6).

Results show that glazed curtain walls definitely contribute to strengthening the main structure, adding energy dissipation at the MRF response. This tendency is distinguishable in Tables 5 and 6, reaching a maximum in braces (Figs. 16 and 17) when façade B is installed in MF-02 (up to **15.81%**) and in outriggers (Figs. 18 and 19) when façade B is installed in MF-01 (up to **25.56%**). In Table 7, where the axial force, the bending moment and the shear force results in columns are summarized (data from Figs. 20–25), the mismatch level between MRF and NLTHA Avg values is maximum. Specifically, when façade B is fastened to the 30-storey frame, the bending moment and the shear percentage attenuation (Figs. 24 and 25) reach **36.78%** and **66.94%**, respectively. Furthermore, since outriggers induce a sharp variation in lateral stiffness of adjacent floors, prominent stress discontinuities arose in columns: appropriate evaluations should be done when the connection systems are under design.

As a result, the case-study structural response emphasizes the importance of ensuring uniformly distributed excess-strength design ratios along the building height, in order to supply distributed dissipative effects and to prevent concentrated forces in single floors.

4.2. Global performance

In this section, the response of the overall structure is Figs. 26 and 27, the response of MF-01 and MF-02 is depicted, both for Façade A and B, in terms of displacements and inter-storey drifts. Peak values of NLTHa Avg are summarized in Table 8. The displacement response adopts a coarse cantilevered shape, while a notable inter-storey drift reduction is visible every 15 storey, due to the stiffening effect induced by the outriggers. The recorded fundamental periods of MF-01 and MF-02 are, respectively, 1.75 s and 4.16 s, thus highlighting a stiffer behaviour of the former (reflected on the maximum base acceleration, 0.59 g for the former and 0.35 g for the latter). Moreover, according to Table 8, the MRF response is higher than NLTHA Avg, underlining the dynamic properties of curtain walls in limiting the structural flexibility up to **4.94%** and **8.17%** with façade B. It is noteworthy that different façades influence the structural deformation likewise, depending on the mechanical reaction of the façade itself.

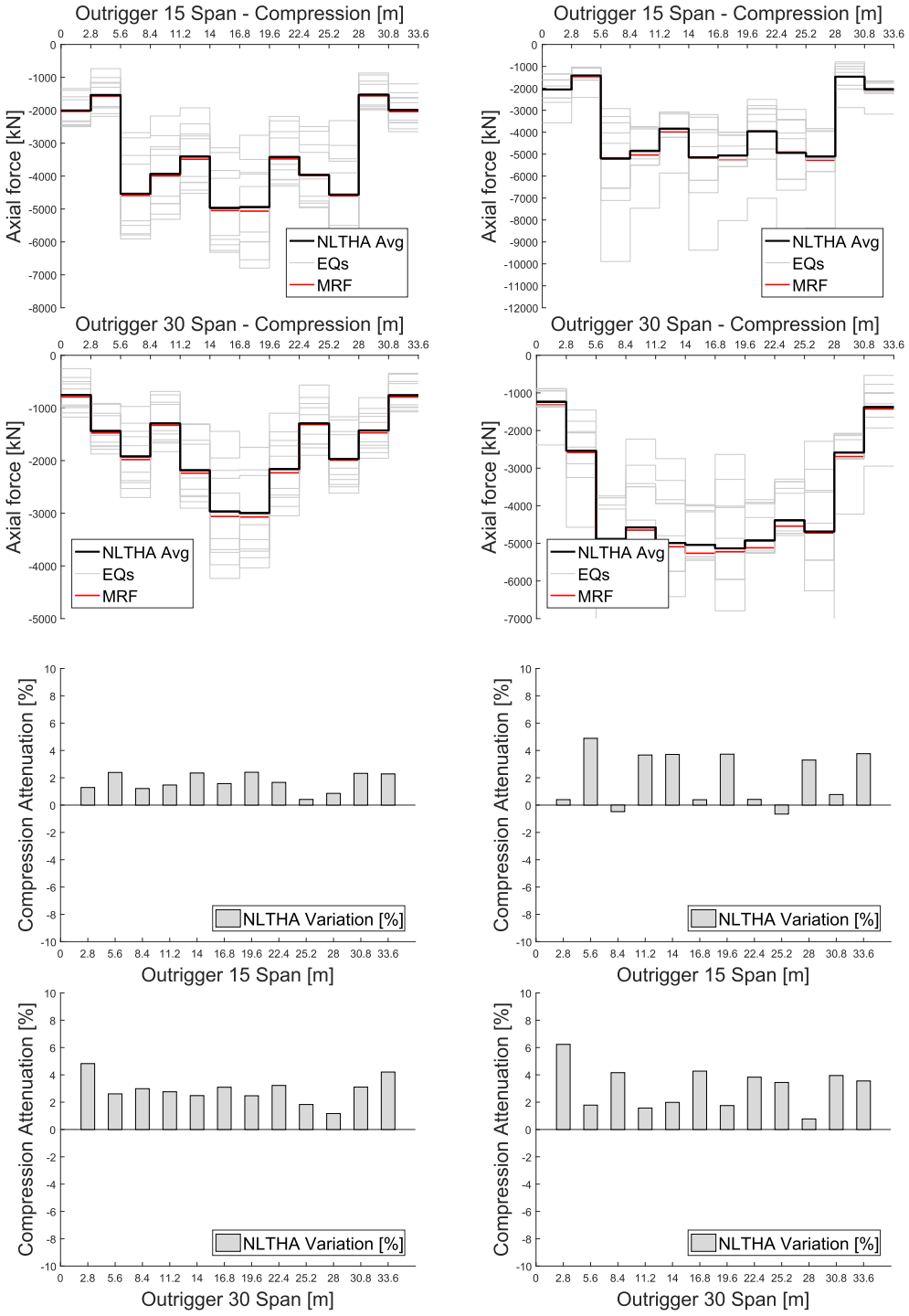

Fig. 18. FAÇADE A - Axial force profile in outrigger & compression variation, MF-01 (left) and MF-02 (right).

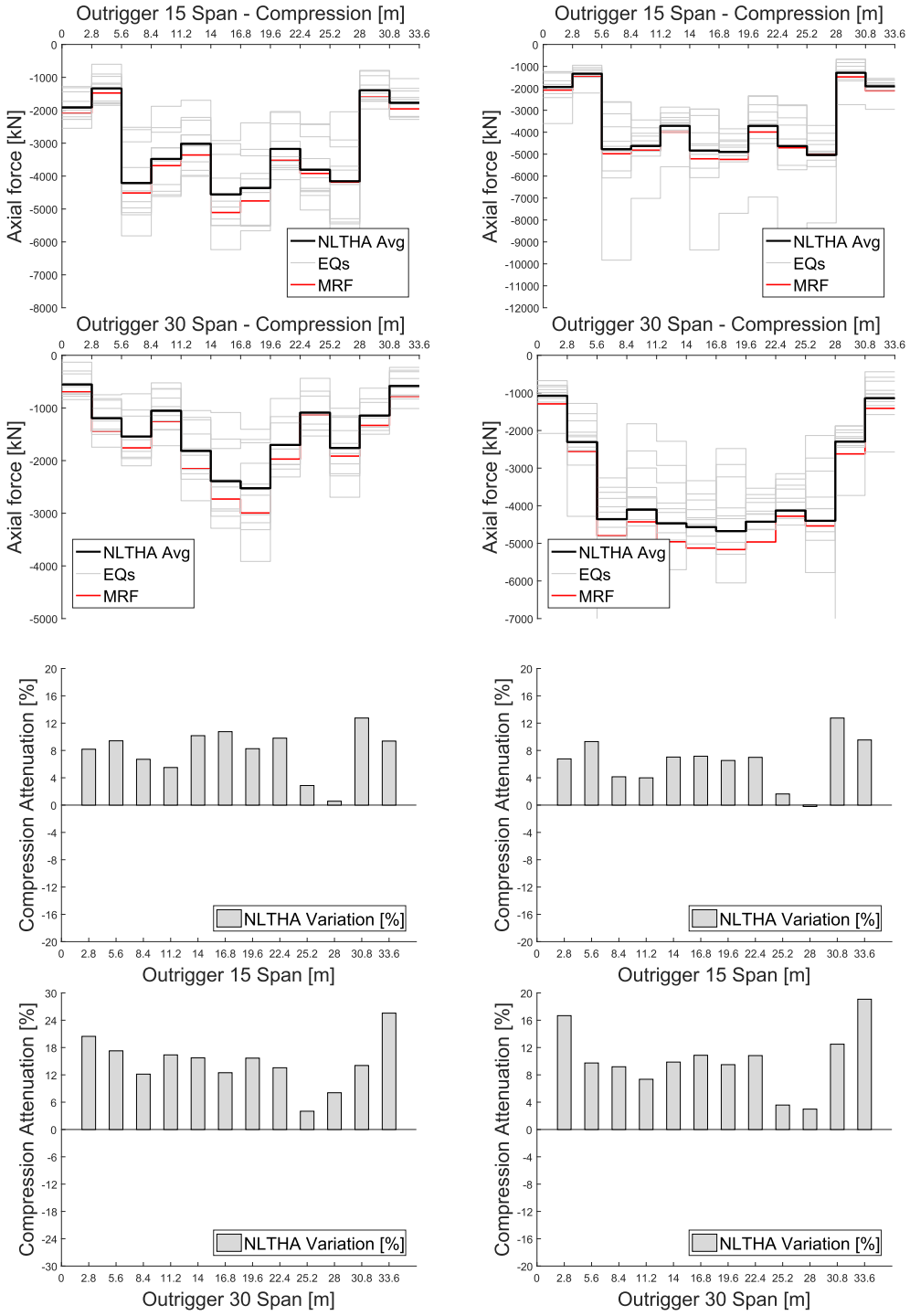

Fig. 19. FAÇADE B - Axial force profile in outrigger & compression variation, MF-01 (left) and MF-02 (right).

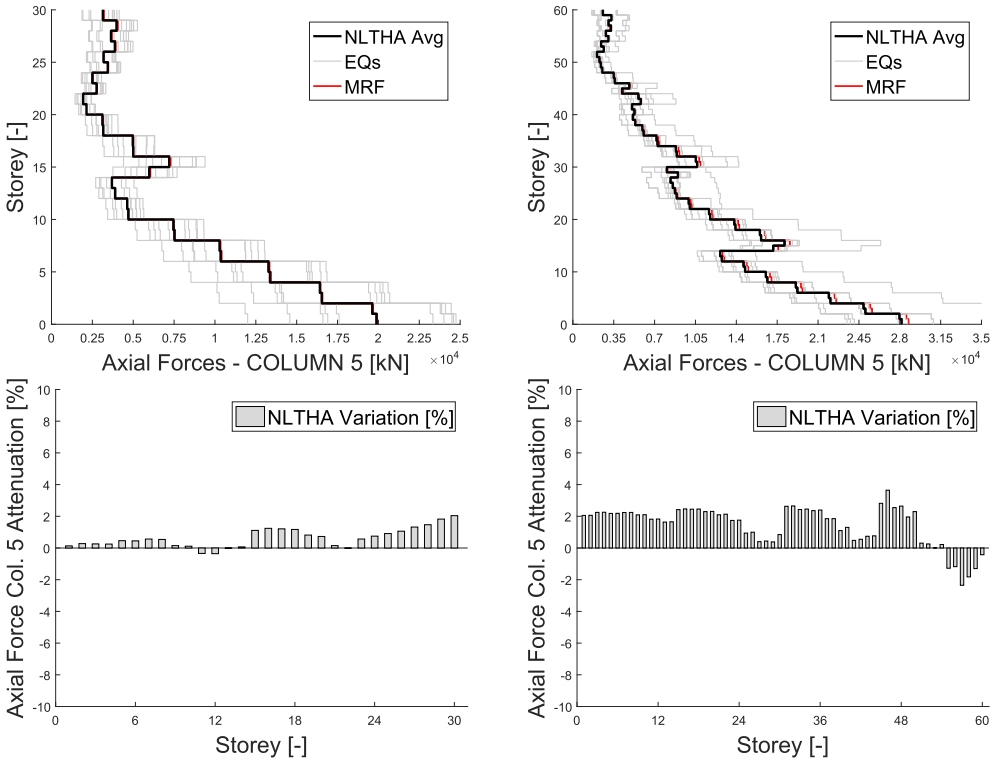

Fig. 20. FAÇADE A - Axial force peak profile in the rightmost core column & compression variation, MF-01 (left) and MF-02 (right).

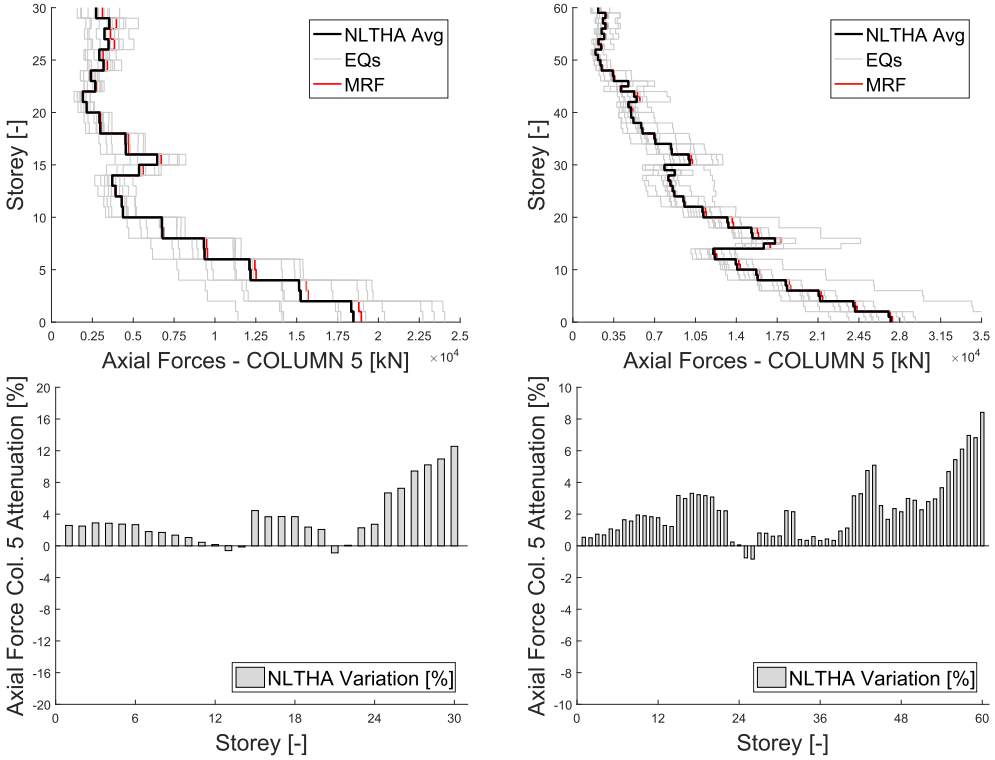

Fig. 21. FAÇADE B - Axial force peak profile in the rightmost core column & compression variation, MF-01 (left) and MF-02 (right).

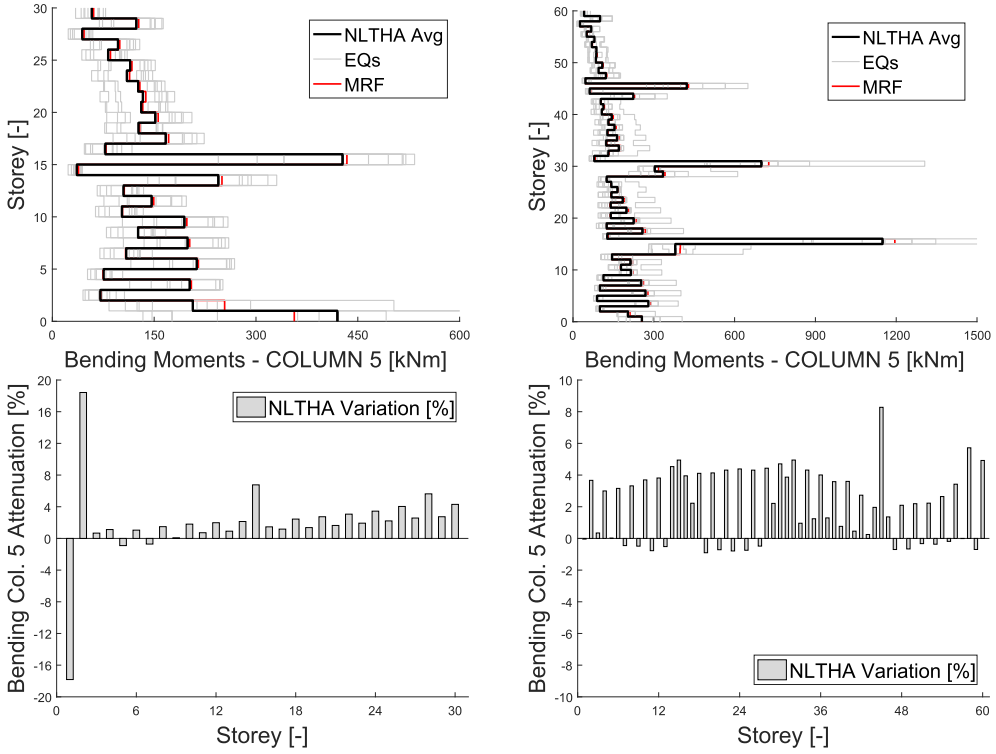

Fig. 22. FAÇADE A - Bending moment peak profile in the rightmost core column & percentage variation, MF-01 (left) and MF-02 (right).

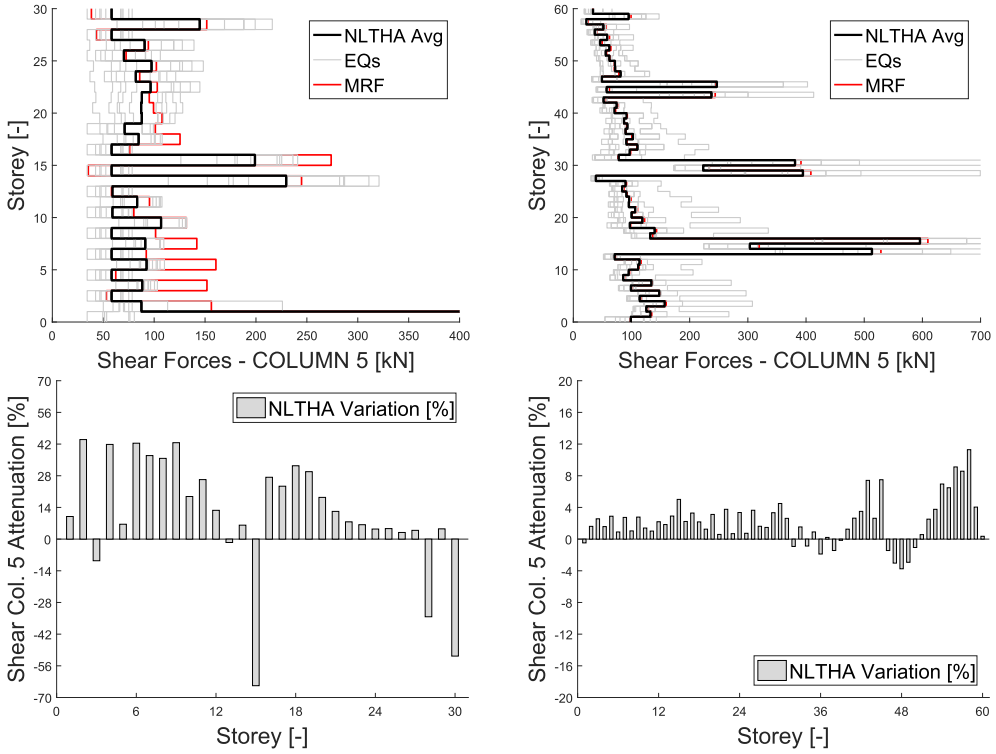

Fig. 23. FAÇADE A - Shear force peak profile in the rightmost core column & percentage variation, MF-01 (left) and MF-02 (right).

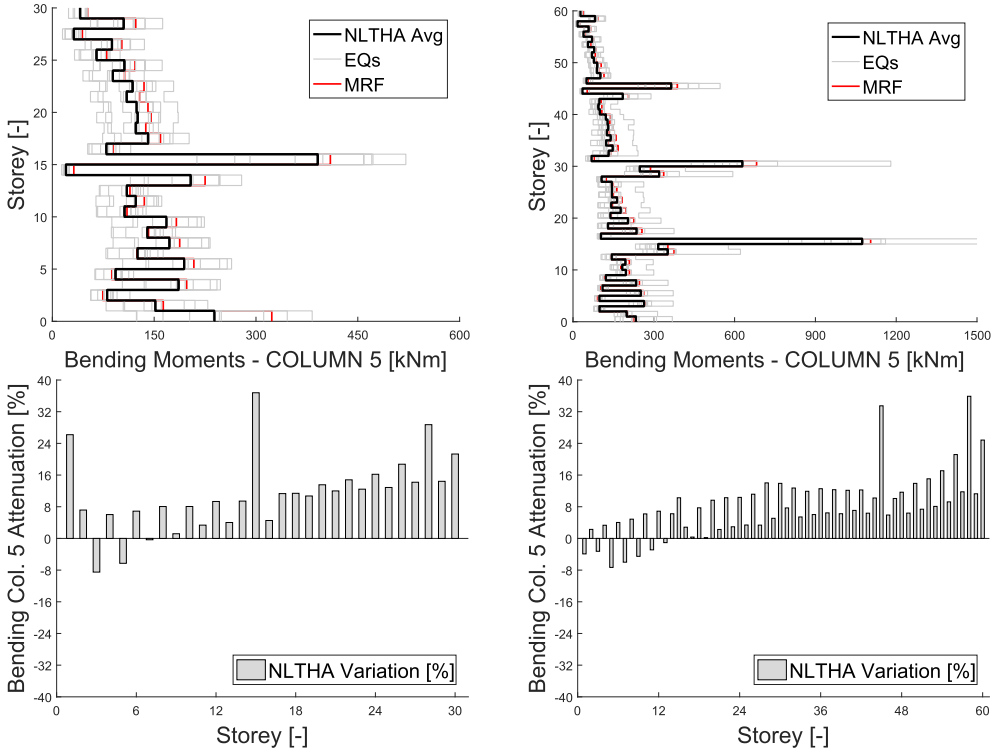

Fig. 24. FAÇADE B - Bending moment peak profile in the rightmost core column & percentage variation, MF-01 (left) and MF-02 (right).

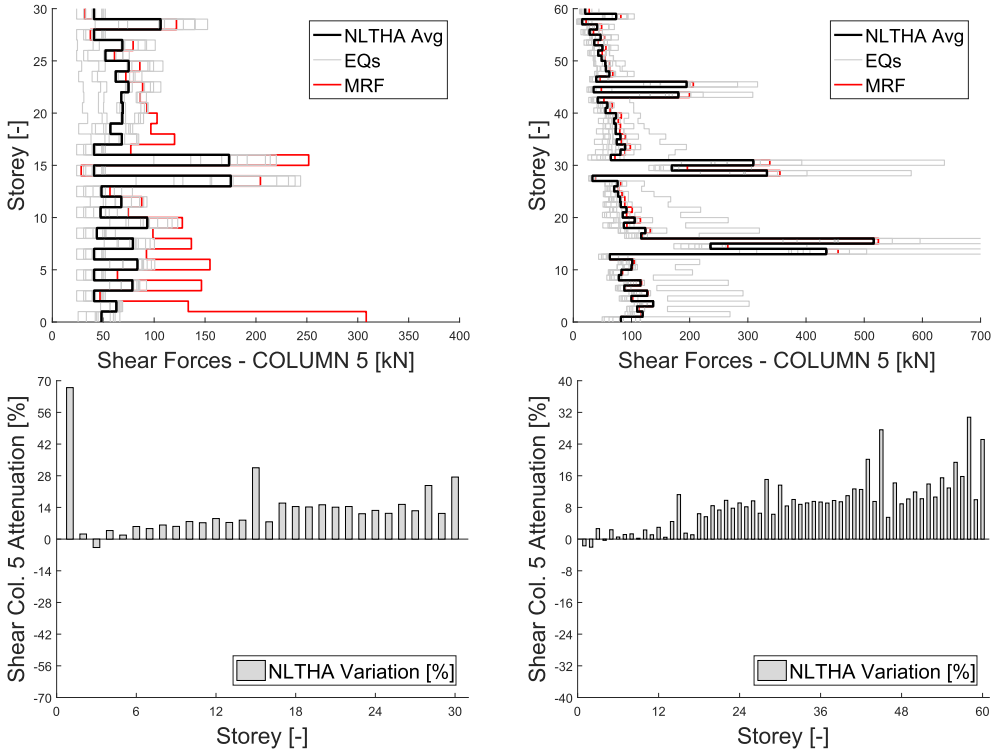

Fig. 25. FAÇADE B - Shear force peak profile in the rightmost core column & percentage variation, MF-01 (left) and MF-02 (right).

Table 5
NLTHa Avg peak values in Façade A and Façade B: braces.

Local Performance	FAÇADE A		FAÇADE B	
	30-storey	60-storey	30-storey	60-storey
Right Brace Axial Force	4968 kN	5039 kN	4369 kN	4482 kN
Right Brace Axial Force Attenuation	3.09%	7.02%	12.47%	**15.81%**

Table 6
NLTHa Avg peak values in Façade A and Façade B: outriggers.

Local Performance	FAÇADE A		FAÇADE B	
	30-storey	60-storey	30-storey	60-storey
15° Outrigger Axial Force	4968 kN	5039 kN	4369 kN	4482 kN
30° Outrigger Axial Force	2995 kN	4903 kN	2122 kN	4144 kN
15° Outr. Axial Force Attenuation	2.41%	4.89%	**12.75%**	12.74%
30° Outr. Axial Force Attenuation	4.83%	6.23%	**25.56%**	19.07%

Table 7
NLTHa Avg peak values in Façade A and Façade B: columns.

Local Performance	FAÇADE A		FAÇADE B	
	30-storey	60-storey	30-storey	60-storey
Column Axial Force	19886 kN	28162 kN	18468 kN	27223 kN
Column Bending Moment	427 kNm	1150 kNm	391 kNm	1073 kNm
Column Shear Force	270 kN	595 kN	232 kN	516 kN
Col. Axial Force Attenuation	2.04%	3.65%	**12.55%**	8.42%
Col. Bending Moment Attenuation	18.43%	7.65%	**36.78%**	35.89%
Col. Shear Force Attenuation	43.99%	11.29%	**66.94%**	30.78%

Results show that, if accurately designed, the chosen structural system provides an excellent balance between stiffness and robustness. When the structural height increases, the planar rotation tends to diminish, resulting in an attenuation of the axial forces involved.

5. Conclusions

An equivalent 1D nonlinear dynamic modelling procedure is herein proposed to speedily quantify the seismic assessment of traditional glazed curtain wall stick systems. This approach, developed on a theoretical basis and validated by numerical and empirical results, is comprehensive and applicable in any type of computational framework, working in a general domain and employing well-known FE standard objects.

Initially, NLTHAs are performed on four nonlinear fiber-based structural prototypes, respectively with thirty- and sixty-storey, derived from a previously designed high-rise three-dimensional frame system (Section 3.1). Subsequently, two glazed curtain wall typologies are modelled (Section 3.2) in order to quantify their influence in the thirty- and sixty-storey structural seismic response. Accordingly, simulations are executed on hybrid systems, obtained by implementing equivalent 1D façades on the moment resisting frames (Sections 3.3 and 3.4). Finally, both global and local performance of the reference mega-frame hybrid-systems are examined (Section 4), leading to these main conclusions:

- reverberation on local and global response is induced by glazed curtain wall employment in the LRFS, attenuating global displacements and internal forces up to **4.94%** and **66.94%**, respectively;
- the dissipation effectiveness of façades should be considered during the design phase, promoting regularity along the structural height. In detail, these mainly show their beneficial effect attenuate lateral loads (shear and bending moments in columns Table 7);
- sensitivity to the façade typology is explored. In this study, façade B mainly influence the structural response in terms of global and local behaviour, principally due to its dynamic assessment, Fig. 12. In this regard, a rational approach should be pursued under the capacity design concepts and the performance-based principles, toward a balance between structural demand reduction and non-structural ductility;
- the structural deformation is composed by the coupled effect of a global lateral sway (due to shear forces) and an overall rotation (owed to base bending moments). As the structural height increase, the amount due to the former decrease respect to the latter. Hence, the façade dissipation is strictly related to the frame elevation: lateral displacements, compression in outriggers and columns, as well as shear forces and bending moments are mainly affected by curtain walls in MF-01; axial forces in braces are mainly reduced by façades in MF-02;
- authors firmly believe that the simplified modelling technique consistently simulates the façade system performance, thus applicable to design processes, vulnerability and quantitative risk assessment, as well as test pre- and post-diction. In addition, the model can be implemented in a probabilistic framework, approaching the shortcomings in current seismic codes.

We want to stress the importance of connections, primarily:

- façade-to-structure joints, have to be conservatively designed to withstand lateral loads generated by inter-storey drift (Fig. 4);
- transom-to-mullion local stiffness should be balanced, moving the vulnerability from the aluminum frame (when rigid, as in Fig. 8(a)) to glazed elements (when nominally pinned, as in Fig. 8(b));
- glass-to-frame joints, due to the presence of gaskets control the initial and the plastic branch slope in backbone responses of curtain wall. As a result, it should be implemented in modeling scenarios; (Fig. 10);

Further studies are under assessment, pursuant with these results, in order to:

- enhance the curtain wall assessment toward the glazed panel fracture prevention when under serviceability state loads, especially against daily wind vibrations;
- optimize the location of outer columns, i.e. where the seismic overburden in compression is maximum (as in Fig. 15);
- reinforce the proposed modelling tool used to predict force-displacement diagrams of façcades performing more experimental analyses and numerical campaigns;
- design innovative devices to improve curtain wall dynamic dissipation.

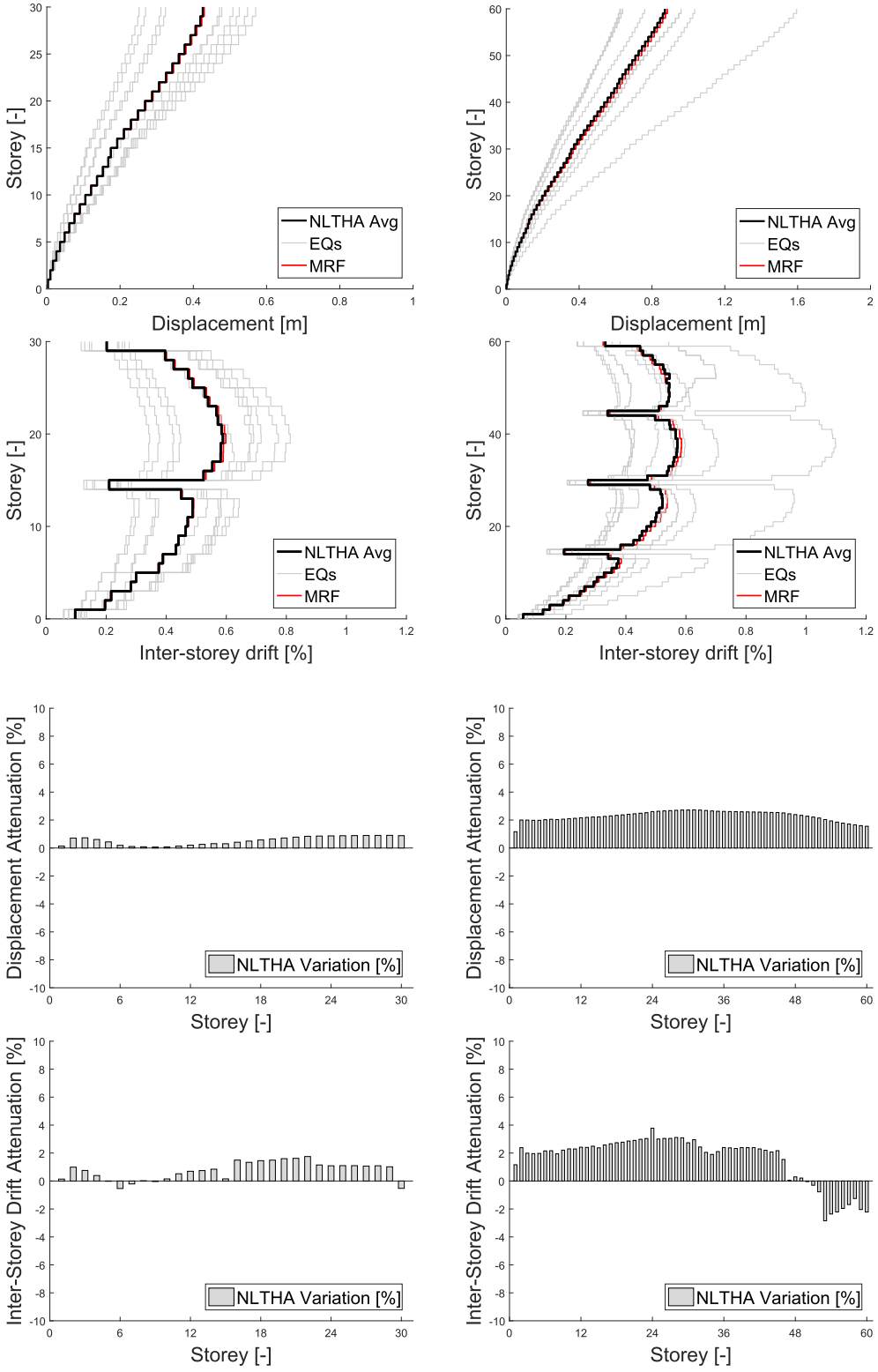

Fig. 26. FAÇADE A - Displacement profile & Inter-storey drift, with related percentage variations, MF-01 (left) and MF-02 (right).

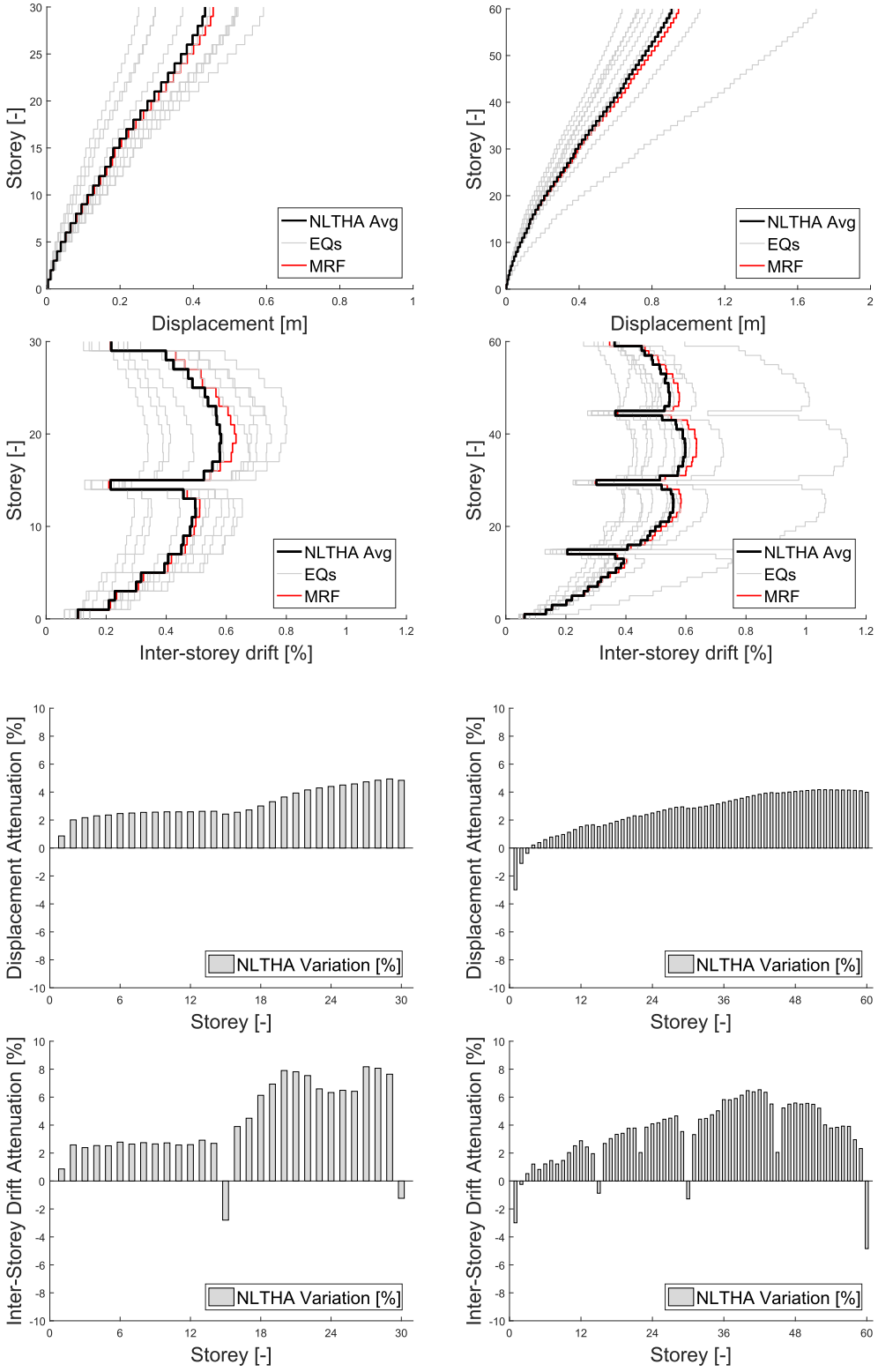

Fig. 27. FAÇADE B - Displacement profile & Inter-storey drift, with related percentage variations, MF-01 (left) and MF-02 (right).

Table 8
NLTHa Avg peak values in Façade A and Façade B: global performance.

Global Performance	FAÇADE A		FAÇADE B	
	30-storey	60-storey	30-storey	60-storey
Displacement	0.426 m	0.872 m	0.408 m	0.854 m
Inter-storey Drift	0.59%	0.57%	0.55%	0.55%
Displacement Attenuation	0.92%	2.72%	**4.94%**	4.17%
Inter-storey Drift Attenuation	1.75%	3.78%	**8.17%**	6.53%

Appendix A. Supplementary material

Supplementary data associated with this article can be found, in the online version, at https://doi.org/10.1016/j.engstruct.2018.10.086.

References

[1] Fan H, Li QS, Tuan AY, Xu L. Seismic analysis of the world's tallest building. J Constr Steel Res 2009;65:1206–15.
[2] Lu X, Lu X, Guan H, Zhang W, Ye L. Earthquake-induced collapse simulation of a super-tall mega-braced frame-core tube building. J Constr Steel Res 2013;82:59–71.
[3] Lu X, Lu X, Sezen H, Ye L. Development of a simplified model and seismic energy dissipation in a super-tall building. Eng Struct 2014;67:109–22.
[4] Montuori GM, Mele E, Brandonisio G, De luca A. Secondary bracing systems for diagrid structures in tall buildings. Eng Struct 2014;75:477–88.
[5] Montuori GM, Mele E, Brandonisio G, De luca A. Design criteria for diagrid tall buildings: stiffness versus strength. Struct Des Tall Spec Build 2014;23:1294–314.
[6] Attanasi G, Auricchio F, Fenves GL. Feasibility Assessment of an Innovative Isolation Bearing System with Shape Memory Alloys. J Earthq Eng 2009;13:18–39.
[7] Welch DP, Sullivan TJ, Calvi GM. Developing direct displacement-based procedures for simplified loss assessment in performance-based earthquake engineering. J Earthq Eng 2014;18:290–322.
[8] Xue Q, Chen C. Performance-based seismic design of structures: a direct displacement-based approach. Eng Str 2003;25:1803–13.
[9] Brunesi E, Nascimbene R, Casagrande L. Seismic analysis of high-rise mega-braced frame-core buildings. Eng Struct 2016;115:1–17.
[10] Li CS, Lam SSE, Zhang MZ, Wong YL. Shaking table test of a 1:20 scale high-rise building with a transfer plate system. J Struct Eng ASCE 2006;132:1732–44.
[11] Lu XL, Zou Y, Lu WS, Zhao B. Shaking table model test on Shangai world financial center tower. Earthq Eng Struct Dyn 2007;36:439–57.
[12] Ayres JM, Sun TY. Nonstructural Damage,The San Fernando California Earthquake of February 9, 1971, US Dep of Comm. Nat Ocean and Atm Adm 1973;1(B):736–42.
[13] Taghavi S, Miranda E. Seismic performance and loss assessment of nonstructural building components. Proc of 7th Nat Conf on Earthq Eng; 2002.
[14] Biggs JM, Roesset JM. Seismic analysis of equipment mounted on a massive structure. Seism Des Nuc Plants 1970:319–43.
[15] Filiatrault A, Sullivan T. Performance-based seismic design of nonstructural building components: The next frontier of earthquake engineering. Earthq Eng & Eng Vib 2014;13:17–46.
[16] Pantelides CP, Behr RA. Dynamic in-plane racking tests of curtain wall glass elements. Earthq Eng Struc Dyn 1994;23(2):211–28.
[17] Behr RA, Belarbi A, Culp JH. Dynamic racking tests of curtain wall glass elements with in-plane and out-of-plane motions. Earthq Eng Struc Dyn 1995;24(1):1–14.
[18] Behr RA. Seismic performance of architectural glass in mid-rise curtain wall. J Arch Eng 1998;4(3):94–8.
[19] Caterino N, Del Zoppo M, Maddaloni G, Bonati A, Cavanna G, Occhiuzzi A. Seismic assessment and finite element modelling of glazed curtain walls. Struct Eng Mech 2017;61(1):77–90.
[20] Kim S, D'Amore E. Pushover analysis procedure in earthquake engineering. Earthq Spectra 1999;15:417–34.
[21] Krawinkler H, Seneviratna GDPK. Pros and cons of a pushover analysis of seismic performance evaluation. Eng Struct 1998;20:452–62.
[22] Chopra AK, Goel RK. A modal pushover analysis procedure for estimating seismic demands for buildings. Earthq Eng Struct Dyn 2002;31:561–82.
[23] Fajfar P. A nonlinear analysis method for performance based seismic design. Earthq Spectra 2000;16:573–92.
[24] Chopra AK, Goel RK. A modal pushover analysis procedure to estimate seismic demand for unsymmetric-plan buildings. Earthq Eng Struct Dyn 2004;33:903–27.
[25] Santagati S, Bolognini D, Nascimbene R. Strain life analysis at low-cycle fatigue on concentrically braced steel structures with RHS shape braces. J Earthq Eng 2012;16:107–37.
[26] Khalfi Y, Houari MSA, Tounsi A. A refined and simple shear deformation theory for thermal buckling of solar functionally graded plates on elastic foundation. Int J Comput Methods 2014;11(5):135007.
[27] Latour M, Piluso V, Rizzano G. Cyclic modeling of bolted beam-to-column connections: component approach. J Earthq Eng 2011;15:537–63.
[28] Brunesi E, Nascimbene R, Rassati GA. Response of partially-restrained bolted beam-to-column connections under cyclic loads. J Constr Steel Res 2014;97:24–38.
[29] Spacone E, Filippou FC, Taucer FF. Fibre beam-column model for non-linear analysis of RC frames: Part 1. Forumlation. Earthq Eng Struc Dyn 1996;25:711–25.
[30] EN 1998-1[2005]. Eurocode 8 (EC8) Design of structures for earthquake resistance - Part 1: General rules, seismic actions and rules for buildings, UNI EN 1998-1, Directive 2004/18/EC.
[31] ASCE 7-05. Minimum design loads for buildings and other structures. Reston (VA): American Society of Civil Engineers; 2006.
[32] SAP2000. Linear and nonlinear static and dynamic analysis and design of threedimensional structures, Berkeley (CA): Computers and Structures Inc.
[33] Casagrande L, Bonati A, Auricchio F, Occhiuzzi A. Dissipating effect of glazed curtain wall stick system installed on high-rise mega-braced frame-core buildings under nonlinear seismic excitation. Proc. COMPDYN 2017, DOI: https://doi.org/10.7712/120117.5677.17166.
[34] Consiglio Nazionale delle Ricerche (CNR). Istruzioni per la Progettazione, l'Esecuzione ed il Controllo di Costruzioni con Elementi Strutturali di Vetro, CNR-DT 210/2013.
[35] Memari AM, Shirazi A, Kremer PA. Static finite element analysis of architectural glass curtain walls under in-plane loads and corresponding full-scale test. Struct Eng Mech 2007;25(4):365–82.
[36] Bouwkamp JG. Behavior of window panels under in-plane forces. B Seismol Soc Am 1961;51(1):85–109.
[37] American Architectural Manufacturers Association (AAMA). Recommended Dynamic Test Method for Determining the Seismic Drift Causing Glass Fallout from a Wall System, Pub. No. AAMA 501.6-09; 2009.
[38] Building Seismic Safety Council. NEHRP Recommended provisions for seismic regulations for new buildings and other structures (FEMA 450), National Institute of Building Sciences, BSSC; 2004.
[39] Architectural Institute of Japan Japanese Architectural Standard Specification JASS 14: Curtain Wall, Japanese Standard Association, AIJ; 1996.
[40] Maley TJ, Roldan R, Lago A, Sullivan TJ. Effects of response spectrum shape on the response of steel frame and frame-wall structures. Pavia (Italy): IUSS Press; 2012.
[41] Mazzoni S, McKenna F, Scott MH, Fenves GL, Jeremic B. Open System for Earthquake Engineering Simulation (OpenSees) 2003 - Command Language Manual.
[42] Uriz P, Filippou FC, Mahin SA. Model for cyclic inelastic buckling for steel member. J Struct Eng ASCE 2008;134:619–28.
[43] Priestley MJN, Grant DN. Viscous damping in seismic design and analysis. J Earthq Eng 2005;9:229–55.
[44] ABAQUS 6.14. Documentation, Dassault Systmes Simulia Corp, Providence, RI, USA; 2016.
[45] Flanagan DP, Belytschko T. A uniform strain hexahedron and quadrilateral with orthogonal hourglass control. J Num Meth Eng 1981;17(5):679–706.
[46] Eurocode 3 (EC3):Design of steel structures. General rules and rules for buildings, UNI ENV 1993-1-1; 1992.
[47] Coelho AMG. Rotation capacity of partial strength steel joints with three-dimensional finite element approach. Comp Struct 2013;116:88–97.
[48] Bouc R. Mathematical model for hysteresis., Report to the Centre de Recherches Physiques; 1971. p. 16–25.
[49] Wen YK. Method for random vibration of hysteretic systems. J Eng Mech Div 1976;102(EM2):249–63.
[50] NZS 1170-5 (S1): Structural design actions - Part 5: Earthquake actions - New Zealand Commentary, Standards New Zealand; 2004.
[51] Villaverde R. Seismic design of secondary structures: state of the art. J Struct Eng 1997;123(8):1011–9.
[52] Weggel CD, Zapata BJ, Kiefer MJ. Properties and dynamic behavior of glass curtain walls with split screw spline mullions. J Struct Eng 2007;133:1415–25.
[53] Weggel CD, Zapata BJ. Laminated glass curtain walls and laminated glass lites subjected to low-level blast loading. J Struct Eng 2008;134:466–77.